Transportation Geotechnics 42 (2023) 101051

Contents lists available at ScienceDirect

Transportation Geotechnics

journal homepage: www.elsevier.com/locate/trgeo

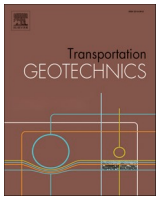

Geotechnical characterization of a novel material obtained by injecting a closed cell expansive polyurethane resin into a sand mass

Luís Miranda [a,*], Laura Caldeira [a], João Bilé Serra [a], Rui Carrilho Gomes [b]

[a] Geotechnics Department, Laboratório Nacional de Engenharia Civil, Av. do Brasil, 101, 1700-111 Lisboa, Portugal
[b] CERIS, Department of Civil Engineering, Instituto Superior Técnico, Universidade de Lisboa, Av. Rovisco Pais, 1049-001 Lisboa, Portugal

ARTICLE INFO

Keywords:
Closed cell expansive polyurethane resin
Sand mass
Injection
Ground improvement
Laboratory testing

ABSTRACT

This paper reports the findings of experimental studies on a novel application of a closed cell expansive polyurethane resin injection into a sand mass, regarding some common engineering properties.

Previous papers on injecting expansive polyurethane resins into sand masses as mitigation measures of different hazards, e.g., liquefaction, settlements and seismic displacements, deal with the open cell sub-class of polyurethane resins. Seeking to make up for the shortcomings of open cell methods, the paper addresses a prototype application of a closed cell polyurethane resin for ground improvement/control on sands.

A new system for the preparation of the sand-resin mixture (SRM), which mimics the field application conditions, is introduced. It allows to inject the polyurethane resin into saturated sand with a prescribed mass density.

The results of an extensive laboratory testing program are presented and discussed regarding some relevant engineering properties, e.g., Young's modulus, Poisson's ratio, uniaxial compressive strength and peak and residual friction angles. Namely, it was concluded that the SRM may be studied as a soft rock and that it shows an essentially plastic behaviour for large deformations, as well as a high shear strength and low permeability.

It is envisaged that these fundamental results may encourage and assist the execution of in situ tests under controlled conditions, concerning the resin injection and its performance assessment, further promoting the application of closed cell polyurethane resins in geotechnical practice in a near future.

Introduction

The relevance of ground improvement or control techniques in geotechnical practice keeps being enlarged due to the scarcity of geotechnical sites of good quality and to the growing tendency of the dimensions and complexity of geotechnical construction projects.

In the field of geotechnical earthquake engineering, a significant use of improvement techniques of granular soils is related mainly with soil liquefaction hazard [21] and, with less relevance, with seismic isolation.

Large earthquakes such as the 1995 Kobe in Japan [50] or the 2010 Chilean earthquake [56] triggered serious damages due to the significant extent and depth of the soil liquefaction phenomena. A recent earthquake sequence with relatively low magnitude in the Emilia-Romagna region [25] produced substantial damage to the buildings due to bearing capacity loss of the saturated alluvial foundation soil.

The seismic isolation of the structures' foundation may be obtained through the judicious definition of target ground properties following its improvement, e.g., by grouting techniques [36] or polyurethane injection foam [16]. The conventional hazard mitigation methods include:

- densification of in-situ soils by, e.g., vibro-replacement [7], vibratory compaction [52], stone columns [2], dynamic consolidation and blasting dynamic compaction [18,34,37];
- providing shorter drainage path for faster dissipation of excess pore water pressure through, e.g., vertical gravel drains [8,10,46,48] or prefabricated drains [41];
- soil reinforcement by, e.g., micropiles [28,30], steel sheet piles [1,19,42], discrete columns in general [43];
- soil improvement by, e.g., soil–cement columns [47], biotechnological processes [35,58], deep soil mixing [1,44] and jet-grouting [27];
- grouting by, e.g., chemical grouting, passive site stabilization with colloidal silica grouting [11,14,15], compaction grouting [9];
- replacing liquefiable soils with non-liquefiable soils [33];

* Corresponding author.
E-mail addresses: lmiranda@lnec.pt (L. Miranda), laurac@lnec.pt (L. Caldeira), biles@lnec.pt (J.B. Serra), rui.carrilho.gomes@tecnico.ulisboa.pt (R.C. Gomes).

https://doi.org/10.1016/j.trgeo.2023.101051
Received 21 March 2023; Received in revised form 15 June 2023; Accepted 17 June 2023
Available online 21 June 2023

- structural measures, e.g., deep foundations as piles [12].

According to Towhata [53], in 2004, amongst a total of 650 reported cases of liquefaction mitigation measures, the relative importance of the methods was the following: densification (62.6% of the reports), grouting (24.6%), drainage (12.3%) and ground reinforcement (0.5%). A growing relevance of grouting as compared to the situation in 1993, i.e., 20 of a total of 275 reports (7%), may be noticed.

Recent developments by inducing partial saturation through air injection [59] or biogas injection [20,38] are also to be mentioned.

Injection of expanding polyurethane resins [13,26,40,54] is another advancement with recent progress achievement. Polyurethane polymers are part of a vast family of polymers. Expansive polyurethane resins can be open cell or closed cell. Open cell resins are less dense, having a more porous structure. On the other hand, closed cell resins are denser and more rigid. Its structure is composed of small, tightly packed cells. Expansive polyurethane resins are produced from an exothermic reaction, between a polyol and an isocyanate, during which a great quantity of carbon dioxide is generated, determining the volumetric expansion of the mixture. When the reactive resin is mixed with water there is foaming. In a very short period the mixture hardens, passing from a liquid state to a solid one. The reaction time, during which the reaction between the components of the resin, and also with water, is still occurring, depends on the properties and type of the resin and the catalysts used, and is also controlled by the admixed components temperature [45].

In the presence of a confinement, the expansive capacity of the resin produces some densification of the surrounding soil, as additional material is introduced in it. Besides, other effects, such as improvement in composite stiffness, grain bonding and horizontal stress increase, are also present [40]. The combined effect provides a substantial improvement of ground strength in the injection zone, which is paramount in case of sand masses with liquefaction potential and also to stiffen the ground and mitigate settlements. The injection pressure range in field applications is from 300 kPa to 10 MPa, and it depends on the type of resin being used, the specific ground improvement application, and the equipment being used for injection.

Recently, open cell (elastomeric) polyurethane resins have been used to improve the mechanical properties of the soil and to recover settlements of shallow foundations [26]. In coarse-grained soils, with high hydraulic conductivity, resin penetrates the pores and there is the formation of a bulb of grouted soil, which expands until reaching equilibrium with confining stresses. Expansion volume can reach 15 times the injected volume, depending on soil density, confining pressure and resin type. The looser the soil, the greater the expansion for a given resin mix [54].

Soil consolidation treatment with expansive resins has shown great flexibility, low energy consumption and extremely reduced environmental impacts. This method offers exceptional advantages over the great majority of mitigation methods in urban environments, concerning excessive noise or vibration generated during construction, and also provides a relatively high level of effectiveness compared to possible alternatives, namely for existing structures [13]. Regarding the economical comparison with other ground improvement methods, it would imply not only comparing the price of the resin but also other factors, like the costs of operation, the type and specific characteristics of the structure where it would be applied, the quantity ordered and the manufacturer. Although the cost of the resin may be considerable, albeit controllable by restraining the volume of resin injection, the costs of operation of equipment are lower than most methods.

In a nutshell, Erdemgil et al. [13], Manassero et al. [26], Prabhakaran et al. [40] and Traylen [54] demonstrated that expansive polyurethane resin injection is a viable ground improvement method for liquefaction mitigation, as liquefaction susceptibility was either eliminated or greatly reduced.

The injection of expanding polyurethane resins represents a new technique for mitigation of liquefaction hazard and large amplitude vibration control. It is a promising novel technique whose application in practice requires the demonstration of its effectiveness. This demonstration ought to be implemented, as a first step, through the valuation of its relative merit when compared with the remaining mitigation methods, regarding both advantages and drawbacks. A number of issues may be considered for this purpose, e.g., quality control regarding dimensions and properties, durability, applicability to pre-existent structures, applicability to long linear infrastructures and environmental issues, including energy consumption.

In contrast with the previous works, which used an open cell (elastomeric) resin, a closed cell (duromeric) polyurethane resin, MC-Injekt 2700 L® [29], is studied for the first time for this type of application. Notwithstanding being slightly less expansive, it has a much higher compressive strength and flexural tensile strength (around 5 times higher) and density (at least twice) than the Uretek® [55] open cell (elastomeric) resin.

This paper reports the findings of experimental studies of a novel material, obtained by injecting the MC-Injekt 2700 L® resin into sand in laboratory conditions. These were aimed at reproducing the field processes of injection and expansion of the resin in saturated sand masses, using a convenient geometric scale. The Tagus River sand was chosen for this purpose, due to its high liquefaction potential.

The laboratory testing is described, including the testing plan and the specimen preparation techniques, which are thought specifically for this new application of the resin. The sand-resin mixture (SRM) engineering properties, e.g., Young's modulus, Poisson's ratio, uniaxial compressive strength and peak and residual friction angles are determined and the effect of the injections on the relative density of the Tagus River sand is analysed.

Materials, test plan and preparation of specimens

Materials

Tagus River sand

The alluvial sand from Tagus riverbed was sampled from material dredged nearby the river's mouth, where the maximum river depth is 30 m, and the maximum thickness of the sand layer (a, in Fig. 1) is approximately 50 m. This area is a potential location for an immersed tunnel crossing of the Tagus River, presently under consideration.

In this zone, the Tagus River sand overlays Miocene formations ($M^1_{I,\,II}$, M^2_{III}, $M^2_{IVa,b}$, $M^3_{Va,\,b,\,c}$, $M^3_{VIa,\,b,\,c}$) and Cretaceous units (C^3_c), with increasing stiffness and strength with depth, and a basalt bedrock (b).

The Tagus River sand is a siliceous, clean and poorly graded sand, classified as SP according to the Unified Soil Classification System – ASTM D2487-17 [6]. The dredged material contained a small fraction of shells and small pebbles, which were removed by passing it through the ASTM #10 sieve.

The sand physical characterization comprised: a grain size analysis, determining the solid particles density, G_S, the minimum and maximum dry unit weight $\gamma_{d,min}$ and $\gamma_{d,max}$, according to ASTM D4254-16 [5] and ASTM D4253-16 [4] standards, respectively. The grain size distribution is shown in Fig. 2, while the physical indexes are presented in Table 1.

The in-situ relative density, D_r, of the Tagus River sand was estimated from the blow counts of the SPT sampler, N_{60}, at different depths of a number of boreholes, mainly at the north bank of the river [31]. Based on Skempton [49], an estimated value of D_r of 70% was obtained from the average value of N_{60} of 17 and used as reference value for the laboratory tests in Miranda et al. [32].

The coefficient of permeability of $6x10^{-4}$ m/s was estimated from constant head permeability tests on saturated specimens prepared with D_r of 70% [31].

From the results of triaxial compression tests [31] the critical friction angle of the sand was determined to be 36°. The tangent Young's

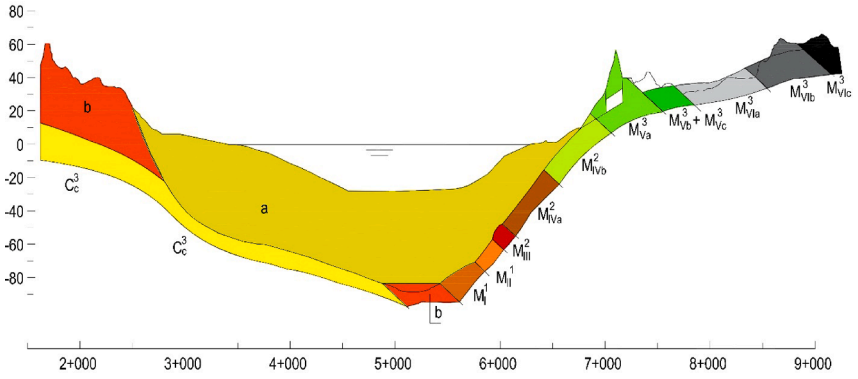

Fig. 1. Geologic profile of the Tagus River bed in the dredging area.

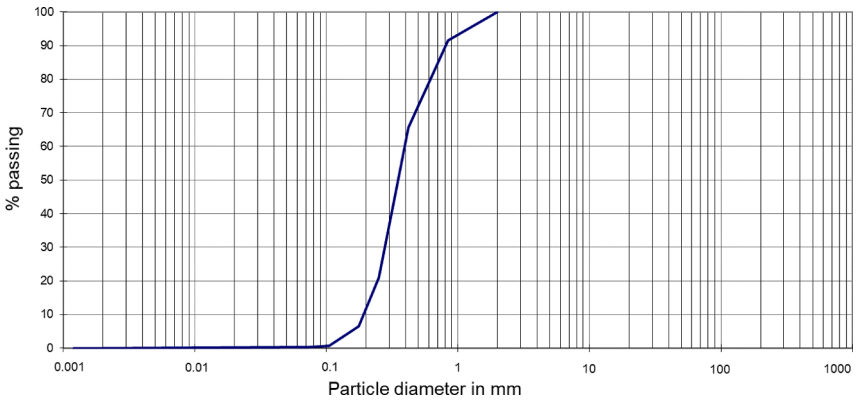

Fig. 2. Grain size distribution for Tagus River sand, after removing particles larger than 2 mm.

Table 1
Physical indexes of Tagus River sand.

Physical index	Value	Physical index	Value	Physical index	Value
D_{10}	0.20 mm	D_{60}	0.40 mm	G_S	2.70
D_{30}	0.28 mm	C_u	2.0	$\gamma_{d,min}$	14.32 kN/m^3
D_{50}	0.36 mm	C_c	1.0	$\gamma_{d,max}$	17.12 kN/m^3

Legend: D_{10}, D_{30}, D_{50} and D_{60} – 10th, 30th, 50th and 60th percentile diameter, respectively; C_u – uniformity coefficient; C_c – curvature coefficient; G_S – solid particles density; $\gamma_{d,min}$ – minimum dry unit weight; $\gamma_{d,max}$ – maximum dry unit weight.

modulus, E, and the Poisson's ratio, ν, for an axial strain close to 0.25%, were estimated to be 132 MPa and 0.3, respectively.

Expansive polyurethane resin MC-Injekt 2700 L®

The MC-Injekt 2700 L® resin is a brownish polyurethane-based resin with low dynamic viscosity (approximately 200 ± 50 mPa.s). It is a closed cell resin with high compressive strength (>75 MPa), and a high flexural tensile strength of around 65 MPa. Its reaction time of about 45 min may be considered as relatively long [29].

It consists of two components (a polyol and an isocyanate), which are mixed with a ratio of 1:1 in the head of an injection pump, and, then, injected with adequate values of pressure and delivery rate. The density of the resin is approximately 1130 kg/m^3. When in contact or mixed with water the resin transforms into a solid and closed cell foam. The reactivity can be controlled by the use of additives. Depending on the confining pressure, the resin can increase its volume up to 10 times with a corresponding reduction in mass density.

It has been applied in sealing and strengthening of cracks, joints and cavities, in structural and underground works, either under dry, wet and high water pressure conditions. Additionally, it has been applied in sealing of sheet piles, diaphragm walls, and leakages in potable water structures.

Test plan

The test plan was designed to characterize the physical, hydraulic and mechanical properties of the SRM material and the densification effect of the injection on the sand adjacent to the expanded SRM columns. The quality and degree of control of the mixing process were also assessed, through the analysis of the average values and dispersion of the dry mass density of the SRM specimens and of their ultrasonic pulse wave velocity.

In order to determine the physical properties of the SRM, the dry mass density, the effective porosity and the maximum water content were measured.

The deformability of the SRM was evaluated by the linear deformation modulus and the Poisson's ratio. The strength properties of the SRM were depicted from the uniaxial compressive and tensile strengths and from the cohesion and the shear strength angle of the Mohr-Coulomb failure criterion in triaxial compression tests. The permeability of the specimens in the triaxial test cell was measured prior to shearing.

The specimens were core drilled from SRM columns, from three sets of samples, each prepared by injection and expansion of the resin in a sand mass deposited by aerial pouring. From sample #1, a total of 17 specimens were prepared, 8 drilled horizontally (1-HB1 to 1-HB8) and 9 drilled vertically (1-VM1 to 1-VM3, 1-VT4 to 1-VT9). From each of the

samples #2 (2-T, M and B) and #3 (3-T, M and B), three specimens were drilled vertically. The tests performed to characterize the SRM material and the estimated parameters on each of the SRM specimens are summarized in Table 2.

Preparation of specimens

Sand samples

The SRM specimens were core drilled from columns of SRM, obtained by injection of resin in saturated sand samples. These samples were prepared by aerial deposition of dry sand from a shower into a cubic container with a 0.5 m internal side, depicted in Fig. 3. Its dimensions were chosen to minimize the boundary effects at the central volume of deposited sand, where the SRM columns would be produced by resin injection. It was constructed in Perspex to allow visual inspection. Bolted connections were used to assemble the walls, and the bottom and top plates [31].

Aiming at the homogenization of the saturation process by upward flow of water, an intake lower chamber was installed underneath the bottom plate of the container. For that purpose, a large number of holes were bored in this plate. Two lateral intake valves at the lower chamber, and four outflow valves at the top plate, were installed.

Fig. 4 shows the shower used to fill the container with sand with a prescribed relative density, in a mechanized and repeatable way [39]. It consists of a parallelepiped deposit with a volume of 0.375 m^3, a drawer-type valve for regulating the sand outflow, a motorized tilting hopper, which spans the area of the container, a sustaining base to the container and a transparent enclosure, with four doors, to limit the propagation of sand dust.

The base of the sand shower deposit has a row of 0.01 m diameter holes in its central zone that match with similar diameter holes of the drawer-type valve in the open position. The pouring flow is prescribed by adjusting this valve to a position previously calibrated as a function of the anticipated dry unit weight. The quasi-translational motion of the hopper is controlled by a hydro-pneumatic system, which enforces a constant rate of swinging oscillation. In order to obtain a uniform deposition of the sand grains, three squared mesh nets exist inside the hopper to minimize the mutual disturbance of their descendent trajectories.

Following the validation of the obtained D_r in the container, its cover was tightened in position and the saturation process was initiated by the upward flow of carbon dioxide gas throughout a four-hour span. During this period, each of the top valves were opened, one at a time, for one hour. The upward percolation of de-aired water under a low hydraulic head followed, as shown in Fig. 5. The intake lower chamber was filled with de-aired water whose percolation through the sand mass progressed from the holes in the interface plate. Each of the four top valves were again opened, one at a time, and the water flow was halted after bubbles stopped exiting the container.

The top plate was, then, removed and a rigid plate was placed so as to cover entirely the sample. The sand was compacted statically under a vertical average stress of 10 kPa imposed by a 2.5 kN weight load on the plate (Fig. 6). This contact stress was kept in position during the injection process in order to enhance the SRM mechanical properties, in

Table 2
Summary data of tests performed for characterizing the SRM properties.

Specimen	Type of test	Parameters	Specimen	Type of test	Parameters
1-VM1	UC, Hf	q_u, E, ν	1-HB4	TC	ϕ_p, c_p, ϕ_r
1-VM2	UC, Hf, P	q_u, E, ν, k	1-HB5		
1-VM3	UC, Hf	q_u, E, ν	1-HB6	UC	q_u, E, ν
1-VT4	UC	q_u, E, ν	1-HB7	UT	σ_{ts}
1-VT5	TC	ϕ_p, c_p, ϕ_r	1-HB8	TC	ϕ_p, c_p, ϕ_r
1-VT6			2-T	TC, Hf	ϕ_p, c_p, ϕ_r
1-VT7			2-M		
1-VT8	UT	σ_{ts}	2-B		
1-VT9	UT		3-T		
1-HB1	UC, Hf, P	q_u, E, ν, k	3-M		
1-HB2	UC, Hf	q_u, E, ν	3-B		
1-HB3					

Legend: 1 to 3 – number of the sample; V/H – vertically/horizontally core drilled specimen; T, M and B stand, respectively, for top, middle and bottom zones of the SRM column from where each specimen was core drilled; UC – uniaxial compression; UT – uniaxial extension; TC – triaxial compression; P – permeability; Hf – High frequency ultrasonic pulse; q_u – uniaxial compressive strength; E – Young's modulus; ν – Poisson's ratio; ϕ_p – peak friction angle; c_p – peak cohesion; ϕ_r – residual friction angle; σ_{ts} – uniaxial tensile strength; k – permeability coefficient.

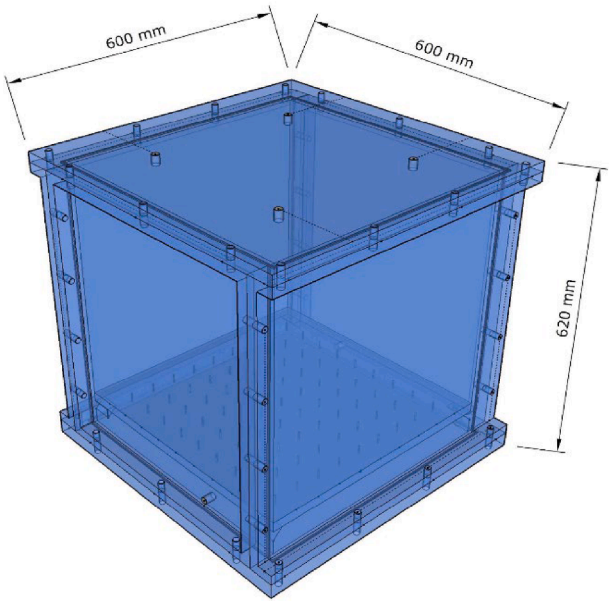

Fig. 3. Perspective drawing of the transparent container.

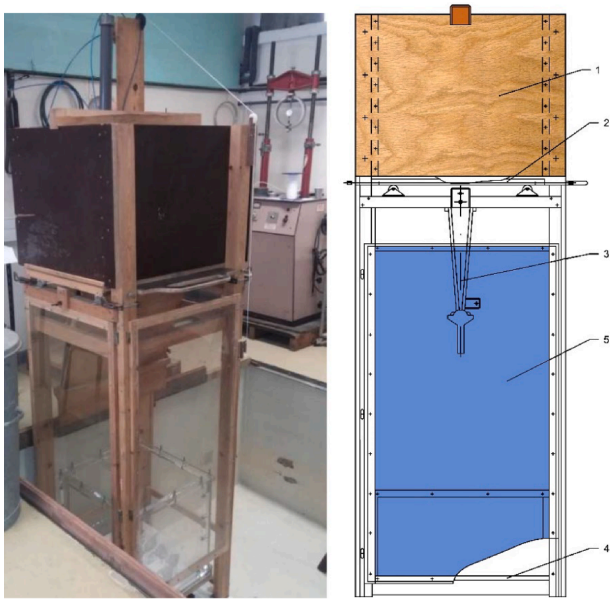

Fig. 4. Quasi-translational sand shower: (a) view with the container in position; and (b) side profile drawing with sand deposit (1), drawer-type valve (2), motorized hopper (3), base (4) and transparent door (5) [39].

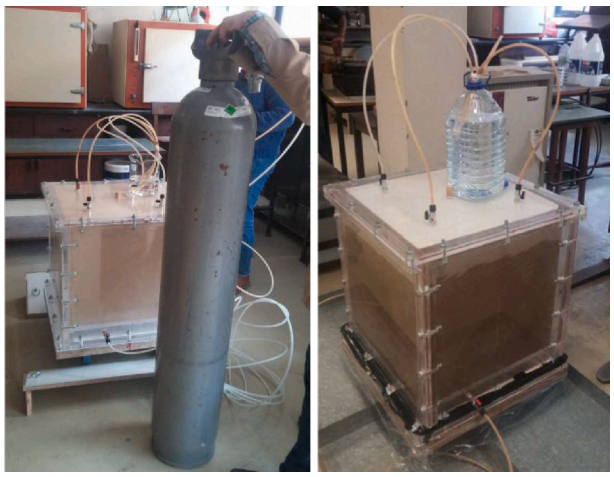

Fig. 5. Carbon dioxide percolation and upward seepage of de-aired water.

Fig. 6. Compaction load configuration (left); injection rod at the central position (right).

agreement with the findings of Traylen [54].

A target value of D_r up to 75% was specified for the poured sand. The relative density D_r of the Tagus River sand was calculated for the three samples along the setup stages, to allow isolating the effect of each stage on D_r (see Table 3). The compaction settlements were measured following the load application and at the end of saturation. The average, δ, of the settlements recorded at the corners and middle points of the edges of the top plate (a total of eight values per reading) was chosen as the representative value of settlement.

Table 3
Data regarding the deposition, saturation and compaction stages of each sample.

Sample	#1	#2	#3
Deposition			
M_S(kg)	207.7	208.2	207.8
γ_d(kN/m^3)	16.28	16.32	16.29
D_r(%)	73.9	75.0	74.0
Saturation			
δ(mm)	1.88	2.66	2.87
γ_d(kN/m^3)	16.35	16.41	16.39
D_r(%)	75.9	77.9	77.1
Compaction			
δ(mm)	2.55	3.70	3.71
γ_d(kN/m^3)	16.37	16.45	16.41
D_r(%)	76.6	79.0	78.0

Legend: M_S - sand mass; γ_d – dry unit weight; D_r – relative density; δ – settlement.

The deposition process proved to be quite repeatable with small dependency to the influence of the operator, given the maximum relative error of 0.4% in the deposited mass and the 0.06 kN/m^3 difference in terms of unit weight.

A total increase of 3–4 % of D_r was obtained, with a major contribution of the collapse due to wetting and particle rearrangement during the saturation phase. The saturation phase settlement represented more than 70% of the total settlement. The small stress of 10 kPa caused a densification expressed by a <1% increase of D_r. Samples #2 and #3 exhibited similar densification response during the saturation and compaction stages while sample #1 was less sensitive to saturation and compaction, due to its slightly more humid initial condition.

Sand-MC-Injekt 2700 L resin mixture samples

Eleven SRM columns (one from sand sample #1 and 5 from each of the sand samples #2 and #3) were prepared with an injection rod, with continuous upward withdrawal. The rod was pushed into the sand to contact the base plate in sample #1 and to a position 3 cm above the base plate in samples #2 and #3. The control variables of the injection were the withdrawal rate of the rod and the injection pressure of the resin. The latter was fixed to the approximate value of 100 kPa, a minimum operational value of the injector nozzle. The withdrawal rate values were selected following trial experiments on the injected column diameter.

In sample #1, a single injection at a central position was achieved to produce enough SRM material for characterization tests. Therefore, a withdrawal rate of 0.11 mm/s was adopted to favour the lateral enlargement of the SRM mass. A SRM column with an enlarged base and with conical shape at the upper and intermediate zones was obtained, as shown in Fig. 7a).

As illustrated in Fig. 8, eight SRM specimens (1-HB1 to 1-HB8, with 0.073 m diameter) were cored drilled in the horizontal direction from the bottom of this column. Three specimens (1-VM1 to 1-VM3, with 0.073 m diameter), from the intermediate zone of the column, and six specimens (1-VT4 to 1-VT9, with 0.050 m diameter), from its upper zone, were core drilled in the vertical direction.

In sample #2, five injection columns were executed in sequence with a withdrawal rate of 1 mm/s, one at the centre of the container and the other four at mid diagonal positions between the centre and each inside corner of the container, with an approximate average diameter of 0.11 m (Fig. 7b)).

Finally, sample #3 was injected with a similar configuration, but with a withdrawal rate of 0.67 mm/s, in order to investigate its effect on the diameter of the columns, and on the densification of the sand exterior to the SRM, i.e., the outlying sand. It is interesting to note that in this case a lower withdrawal rate corresponded to a slightly larger diameter of the columns (average value of 0.12 m), but did not influence the quality of the mixture.

The resin spread in the bottom of each column following the opening of the nozzle, as portrayed in Fig. 7, because of the time delay of the upward movement, at the beginning of the injection process. This situation was more significant in sample #1, since the injection rod was initially placed in contact with the base plate of the container and the withdrawal rate was lower. The conical shape of the columns can be explained as a joint effect of gravity action and viscosity of the resin. Additionally, the columns have a perfectly defined shape, suggesting that the resin was contained at the limits of that shape.

Densification of the outlying sand caused by the resin expansion

The final vertical displacement of the top plate was measured three hours after the injection, following the end of the resin reaction time, deemed to occur 45 min after the injection. The outlying sand was easily excavated with a small shovel, dried and weighed. Visually, it was possible to confirm that the resin was not present among the excavated material. The volume and weight of the SRM material were also

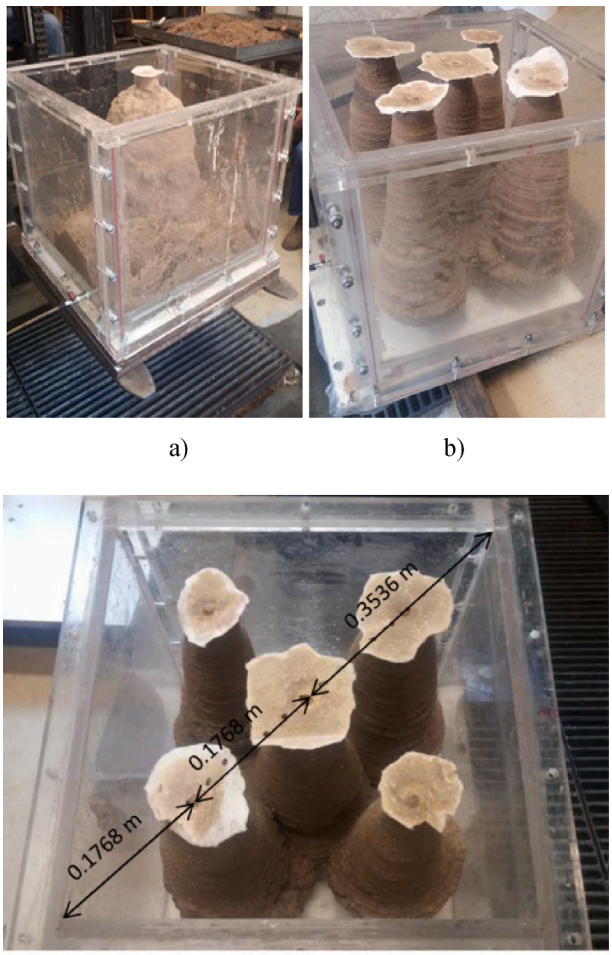

Fig. 7. Configuration of the SRM column(s) in sample: (a) #1; (b) #2; and (c) #3.

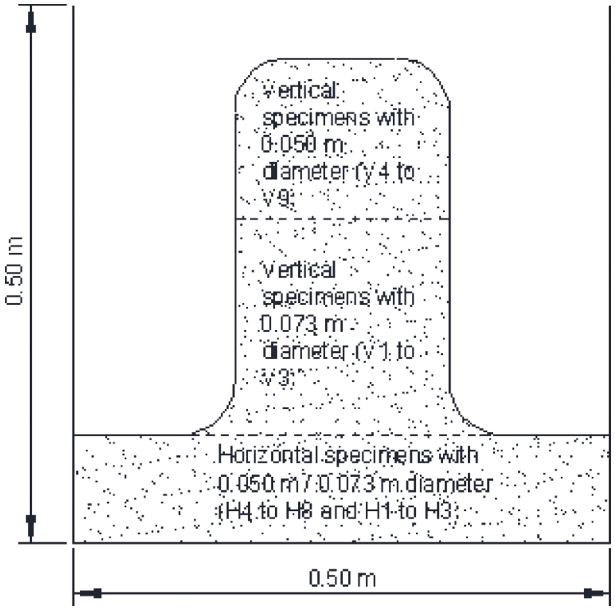

Fig. 8. Scheme of the SRM column core-drilling in sample #1.

measured. By using the dry unit weight of the sand, γ_d, the relative density of the outlying sand could be calculated (Table 4). It was assumed that the sand was completely saturated and that the hydrated resin totally replaced the water in the sand pores. The variation of D_r, expressed as percentage points, is presented in Table 4 for the three samples.

The injection and expansion of the resin in samples #1 and #3 caused 4 mm to 5 mm heave, large enough to invert the settlement at the end of the static compaction. The corresponding increase of D_r of the outlying sand is quite significant (6.1% and 12.1%). In sample #2, however, the injection and expansion were not so effective since the unit weight variation was only 0.01 kN/m^3, i.e., a practically insignificant increase of D_r. The lower withdrawal rate at sample #3 as compared to that of sample #2 caused a major increase in the volume of SRM (only 11.5 L in sample #2 and 18 L in sample #3). Even if the larger volume of the lower zone of the SRM in sample #1 is disregarded, the withdrawal rate of sample #2 was definitely excessive, as the similarity of the replacement ratios of samples #1 and #2 suggests.

Based on estimates of the volume of injected resin and of the volume of hydrated resin mixed with the sand, an estimate was obtained of the expanded volume of resin. Sample #3 not only received the larger volume of injected resin but showed the larger volume expansion ratio of the resin (Table 5). The greater final volume of SRM in sample #3 is cumulatively explained by having received the largest volume of resin and by showing the highest expansion ratio.

The expansion ratio of a given volume of injected resin is a direct consequence of the water availability. Further, the larger contact surface area between the injected volume and the saturated sand favours the expansion outcome. Sample #3 has lower withdrawal rate than sample #2 and a higher contact surface area than sample #1. Therefore, the experimental conditions of sample #3 were the most adequate concerning the densification of the outlying sand.

Had a larger volume of SRM been used, the columns would have overlapped, and their expansion would have been limited by the walls of the container as well. Consequently, D_r would be affected by the boundary conditions, precluding the usage of this container.

Quality control of the injection/mixing process

The quality of the injection/mixing process was assessed by the final conditions of the SRM specimens, namely their dry mass density, ρ_d, and their ultrasonic pulse travel velocity.

Some observations about the homogeneity of the specimens from sample #1 may be formulated from the dry mass density data shown in Table 6. The overall dispersion of ρ_d (V + H = 4%) of the specimens is relatively small considering the physical process involved in the resin expansion. The dry mass density of the horizontal specimens, from the lower zone of the SRM column, is up to 6% less than that of the vertical ones with the same diameter, core drilled from the top of the column. This might be explained by the horizontal specimens having been core

Table 4
Data regarding the injection and expansion phase of each sample.

Sample	#1	#2	#3
Injection and expansion			
Withdrawal rate (mm/s)	0.11	1	0.67
$\delta^{(+)}$ (mm)	−1.53	3.19	−0.99
$\Delta\delta^{(\times)}$ (mm)	−4.08	−0.51	−4.70
Total V (dm^3)	125.51	124.32	125.37
SRM V (dm^3)	30.18	30.04	42.14
Sand V (dm^3)	95.325	94.286	83.236
R_r(%)	24	24	34
γ_d (kN/m^3)	16.56	16.46	16.80
D_r(%)	82.7	79.6	90.1
ΔD_r(%)	6.1	0.6	12.1

Legend: $^{(+)}$ Total increment from deposition condition; $^{(\times)}$ Due solely to resin expansion; *Rr* - replacement ratio, i.e., ratio of the volume of the SRM to the net volume of the container.

Table 5
Variables of the resin expansion.

Sample	Volume of injected resin (L)	Volume of expanded resin (L)	Expansion ratio
#1	9.0	12.8	1.42
#2	5.0	11.5	2.33
#3	7.5	18.0	2.39

Table 6
Dry mass density of the SRM specimens from sample #1: average value and coefficient of variation.

	1-HB1 to 1-HB3	1-HB4 to 1-HB6, 1-HB8	1-HB (all)	1-VM1 to 1-VM3	1-VT4, 1-VT6, 1-VT7	1-VM/T (all)	1-V + 1-H (all)
Diameter (m)	0.073	0.05		0.073	0.05		
Average ρ_d (kg/m^3)	1727	1788	1761	1843	1833	1838	1797
CoV (%)	7.0	2.2	4.6	3.1	2.1	2.4	4.2

drilled farther from the injection axis, therefore with a larger SRM volume per solid angle of the injection front, thus resulting in a lower ρ_d value. The non-uniform expansion of the resin, influenced by the distance from the injection axis, can also explain the higher coefficient of variation in the lower zone of the column, where the SRM occupied a larger volume.

The ultrasonic pulse velocity of P and S sine waves may be used as a comparative measure of the specimens' quality. Two transducers at the tops of the cylindrical specimens were used to transform the electric signal into a mechanical impulse or vice versa. To better identify the shear wave arrival, a sufficient distance between transmitter and receiver was pursued by implementing a minimum value of 2 for the height/diameter ratio of the specimens.

In Table 7, the values of the P and S waves velocities, v_p and v_s, and the derived values[1] of the small strain shear and Young moduli and of the Poisson's ratio, G, E and ν, are displayed for specimens from samples #1 to #3. The estimated values of the wave velocity for sample #1 suggest a small dispersion, i.e., a CoV up to 4.4%. Concerning samples #2 and #3 the dispersion is a little higher, although still small, up to 8% and 11%, respectively. A relative difference of 5% between the horizontal and vertical drilling directions, with larger values of the latter is consistent with the interpretation based on the distance of the specimen to the central axis of the box. It is also interesting to note that the ultrasonic wave velocities, and estimated parameters of linear elastic deformability, are of the same order of magnitude for all the specimens in Table 7, even if core-drilled from columns with different withdrawal rates, which led to a different densification of the sand.

Table 7
Ultrasonic sine wave pulse velocities and estimated parameters of linear elastic deformability.

Specimen	ρ_d(kg/m^3)	v_p(m/s)	v_s(m/s)	G(GPa)	E(GPa)	ν
1-VM1	1907	2423	1470	4.12	9.96	0.21
1-VM2	1827	2579	1494	4.08	10.17	0.25
1-VM3	1796	2544	1387	3.45	8.90	0.29
1-HB1	1844	2645	1524	4.28	10.72	0.25
1-HB2	1733	2739	1556	4.20	10.59	0.26
1-HB3	1604	2509	1462	3.43	8.52	0.24
2-T	1908	2985	1750	5.84	14.46	0.24
2-M	1938	3299	1827	6.47	16.55	0.28
2-B	1863	2835	1575	4.62	11.80	0.28
3-T	1971	2845	1634	5.26	13.19	0.25
3-M	1965	2332	1345	3.55	8.89	0.25
3-B	1819	2510	1357	3.35	8.66	0.29

[1] $G = \rho v_S^2$; $K = \rho v_P^2 - \frac{4}{3}G$; $E = \frac{9KG}{3K+G}$; $\nu = \frac{3K-2G}{6K+2G}$.

Experimental results and analysis

At least seven days after the resin injections, the cylindrical specimens for laboratory testing were core drilled from the SRM columns. Before testing, the specimens were left curing, submerged in water, inside a saturated chamber, for at least another 7 days, as a proxy for the riverbed conditions.

The dimensions, mass density, porosity and maximum water content at the beginning of tests of specimens from samples #1, #2 and #3 are shown in Table 8. The types of tests for each specimen are summarized in Table 2.

Permeability

Regarding the SRM permeability, specimens 1-HB1 and 1-VM2 were chosen for permeability estimation in a triaxial cell [31]. Acted upon by a hydraulic gradient of 6 between the base and the top of the specimens, an average value of 4×10^{-9} m/s was obtained. It is five orders of magnitude less than the sand permeability coefficient, 6×10^{-4} m/s. It is suggested that during the expansion process the resin essentially filled or blocked the access to the voids of the sand.

Uniaxial compression tests

The uniaxial compression tests were performed following the ASTM D7012-14e1 standard [3], relevant for testing of intact rock core specimens. Thus, some adaptations were necessary due to the different test material and equipment used [31].

Wet specimens from sample #1 with both available diameters were tested, i.e., 1-VT4 and 1-HB6 (0.050 m diameter), 1-HB1 to 1-HB3 and 1-VM1 to 1-VM3 (0.073 m diameter). Aiming at studying the influence of humidity on the uniaxial compression response, specifically on q_u, four additional specimens 1-VM2, 1-VM3, 1-HB1 and 1-HB3 (0.073 m diameter) were tested after being dried at the laboratory oven.

Two different loading frames, respectively, a Losenhausen equipment with a load capacity of 50 kN for the 0.050 m diameter specimens and a FORM + TEST Alpha 20–600 equipment, with a load capacity of 600 kN, for the 0.073 m diameter specimens, were used, due to the higher load capacity needed to attain failure in the latter case. Axial loading was applied at constant rate (9 kN/min and 0.8 kN/min, respectively in the former and in the latter frames), the minimum applicable rate at each equipment, to avoid dynamic effects, with one or more cycles of loading–unloading followed by compression until failure attainment. The axial and radial extensions were measured by LVDTs on the middle third of the specimen.

For the 0.073 m diameter specimens, only a single load-unload cycle was considered. The 0.050 m diameter specimens were subjected to three unload-reload cycles to confirm elasticity prevalence inside the yield locus, expanded by plastic hardening during the first cycle. The load amplitude of the cycles was close to one third of the estimated value of q_u obtained from point load testing of similar material.

The tangent linear deformation modulus, E, and the Poisson's ratio, ν, of the SRM specimens were computed during the first loading–unloading cycle of each uniaxial compression test. The estimates of the tangent linear deformation modulus, E, and of the Poisson's ratio, ν, are summarized in Table 9.

In general, the estimates of E and ν were taken equal to the average of the load and unload representative values of the first cycle (e.g., Fig. 9, for specimen 1-VT4). Hence, the tangent Young's modulus, $E(=\Delta\sigma/\Delta\varepsilon_a)$, was estimated in the linear section of the load-unload curves (in red in Fig. 9). The tangent Poisson's ratio, $\nu(=-\Delta\varepsilon_r/\Delta\varepsilon_a)$, was

Table 8
SRM specimens: dimensions and physical properties.

Specimen	H (m)	D (m)	ρ_d(kg/m^3)	n (%)	w_{max}(%)	Specimen	H (m)	D (m)	ρ_d(kg/m^3)	n (%)	w_{max}(%)
1-VM1	0.1514	0.073	1907			1-HB4	0.1148	0.05	1737		
1-VM2	0.1509		1827			1-HB5	0.1198		1815	11.3	6.2
1-VM3	0.1539		1796			1-HB6	0.1209		1777	9.2	5.2
1-VT4	0.1146	0.05	1796	11.4	6.4	1-HB7	0.1182				
1-VT5	0.1133					1-HB8	0.1202		1823	6.3	3.3
1-VT6	0.1142		1830	12.1	6.7	2-T	0.1205	0.05	1863		
1-VT7	0.1134		1873	14.7	8.2	2-M	0.1253		1938		
1-VT8	0.1140					2-B	0.1260		1908		
1-VT9	0.1139					3-T	0.1256		1819		
1-HB1	0.1600	0.073	1844			3-M	0.1256		1965		
1-HB2	0.1603		1733			3-B	0.1156		1971		
1-HB3	0.1594		1604								

Table 9
Uniaxial compression testing: E, ν and q_u values.

Wet condition				Dry condition			
Specimen	E(GPa)	ν	q_u(MPa)	Specimen	E(GPa)	ν	q_u(MPa)
1-VM1	3.52	0.33	24.8	1-VM2	4.50	–	27.0
1-HB2	5.25	0.29	21.9	1-VM3	5.94	0.22	37.8
1-VT4(*)	5.58	0.25	34.4	1-HB1	3.45	0.31	21.1
1-HB6(*)	5.70	0.23	26.9	1-HB3	4.71	0.23	23.0

Legend: (*)0.050 m diameter specimens, unlike the other specimens whose diameter is 0.073 m.

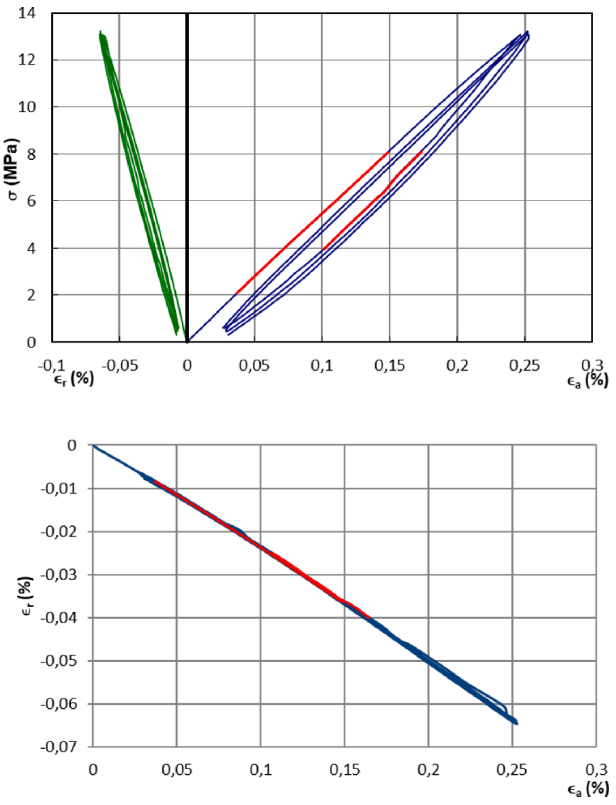

Fig. 9. Uniaxial compression of specimen 1-VT4: axial stress *versus* axial/radial strain and radial strain *versus* axial strain.

calculated from similar axial strain variation intervals. The stability of the shape of the consecutive cycles suggests that for axial strain values less than 0.25% no significant accumulated damage was imposed to the material.

The curves in Fig. 9 may be considered to represent a response pattern of the specimens, except for the two anomalous case of specimens 1-VM1 and 1-HB1. The values of E of the remaining specimens, between 4.5 and 6 GPa, may be considered as normal.

The specimens 1-VM1 and 1-HB1 exhibited much lower values of E, higher values of ν and significant plastic strains. Here, the estimates of E and ν were taken equal to the average of the corresponding values during loading and unloading, as displayed in Fig. 10 for specimen 1-VM1. Although specimens 1-VM1 and 1-VT4 were cyclically loaded to

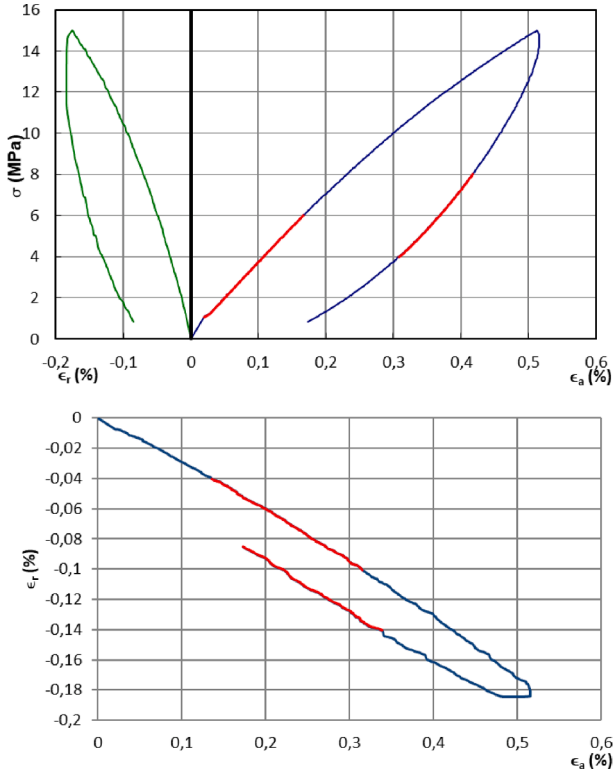

Fig. 10. Uniaxial compression of specimen 1-VM1: axial stress *versus* axial/radial strain and radial strain *versus* axial strain.

maximum loads of similar order of magnitude, it may be observed that the former exhibited significant plastic strains, and a hysteresis area one order of magnitude higher than the later.

The average value of E obtained without consideration of specimens 1-VM1 and 1-HB1 is 5.3 GPa, while the value corresponding to the complete set is 4.8 GPa. The difference of the degree of homogeneity between V and H specimens had no significant influence, either on the average linear deformability modulus (4.88 GPa in the vertical direction *versus* 4.78 GPa in the horizontal direction) or on the average Poisson's ratio (0.27).

In Table 9, the experimental q_u values are also displayed. Considering the full set of specimens in Table 9, i.e., without segregation of wet and dried specimens, it may be perceived that the q_u values of the VM and VT specimens are higher than those of the HB specimens. This may be illustrated by the comparison of the average values, i.e., 31.0 MPa *versus* 23.2 MPa. The fact that the base of the SRM column in sample #1 is the origin zone of the HB specimens, where the spatial distribution of the resin is necessarily poorer than in the narrower middle and top zones, appears to be a determinant factor.

Amongst the wet specimens, the q_u values of the 0.050 m diameter specimens, particularly 1-VT4, are higher than their counterparts of 0.073 m diameter (1-HB2 and 1-VM1). This can be related to the fact that the specimens 1-VT4 and 1-HB6 exhibited a more continuous distribution of the resin, thus forming a stronger material structure, as suggested by Fig. 11. It is possible to observe that specimen 1-VT4 is homogeneous, while failure of the specimen 1-VM1 was accompanied by a crack opening between two zones with constrasting content of resin.

To ascertain whether the differences in the specimens' structure, due to some likely degree of irregularity of the spatial distribution of the resin, could be a determinant factor to the dispersion of q_u and E, optical microscope analyses were performed with an OLYMPUS BX60 microscope. A thin laminar section was taken from specimen 1-VM3 (with the highest q_u, in Fig. 12) and from specimen 1-HB1 (with the lowest q_u, in Fig. 13).

In the left-side pictures of Figs. 12 and 13 it is possible to observe the sand grains in grey. The gluing process of the microscope slides to the specimens created a limited number of small air bubbles (white areas with black outline). In the right-side pictures, taken following the microinjection of fluorescein [23], the light green areas represent the voids (yellowish areas in the left side pictures). The remaining areas denote the space occupied by the resin (light brown areas in the left side pictures). In Fig. 14, a zoom of a selected zone from the laminar section of specimen 1-HB1 is also presented.

When comparing Figs. 12 and 13, a more irregular distribution of the resin, as well as a greater continuity of the voids in specimen 1-HB1 can be noticed, which is a possible explanation for its q_u being the lesser of the two.

Uniaxial extension testing

In the direct uniaxial extension testing, an Instron 5900R frame with a load capacity of 100 kN was used. The specimens were stretched along its longitudinal axis at a constant displacement rate, i.e., 0.1 mm/min, until failure. The specimens were stretched by grips attached to the machine. The standard ISO 527-1:2019 [22], relevant for plastics, was followed with the necessary adaptations, namely concerning the load frame.

The values of the uniaxial tensile strength, σ_{ts}, were 2.0 MPa for specimen 1-VT9 and 3.0 MPa for specimen 1-HB7. The ratio q_u/σ_{ts} is close to 15 for the vertically cored drilled specimen and close to 8 for the horizontally core drilled specimen. This is also considered a manifestation of the different degrees of irregularity in the resin distribution in the V and H specimens.

Triaxial compression tests

Both load-controlled and strain-controlled triaxial compression tests, with constant radial stress were performed. The former aimed at testing the specimens with the same test control type of the uniaxial compression tests. The latter were meant to characterize the post-peak domain of the SRM response. In both types of tests, the same three different values of constant confining pressure (i.e., 0.3 MPa, 1.2 MPa and 2 MPa) were adopted taking into account the high estimates of q_u as above.

Table 10 summarizes the results of the load-controlled triaxial compression tests. They were performed using a SOILTEST load frame with a load capacity of 200 kN. The tests followed the standard ASTM D7012-14e1 [3], with the necessary adaptations due to the different material tested and equipment used.

The specimens were sheared with a constant axial load rate of 9 kN/min until failure was attained, corresponding to the deviatoric stress, q_f , and the concomitant axial strain, $\varepsilon_{a,f}$. The axial strain rate was naturally variable, with smaller values taking place during the initial shearing, due to the current higher values of E. For the sake of comparison analysis with the strain-controlled tests, data of the average axial strain rate, $\dot{\varepsilon}_{a;avg}$, calculated for an axial strain below 0.2%, where the estimates of the Young's modulus were obtained, is also displayed in Table 10.

The strain-controlled tests were performed on specimens from samples #2 (B, M and T) and #3 (B, M and T) with an INSTRON load frame (model SY 5142-1) with a load capacity of 500 kN. In Table 11, the results of the strain-controlled triaxial compression testing are summarized, i.e., the peak deviatoric stress, q_{peak}, the concomitant axial strain, $\varepsilon_{a,peak}$, and the residual deviatoric stress, q_{res}, are presented. The estimates of Young's modulus displayed in Table 11 were obtained for axial strains below 0.2%. The rock mechanics terminology has been adopted, when referring to the ultimate (residual) conditions attained in these tests [57].

A constant axial displacement rate of 0.06 mm/min (i.e., approximately 0.4%/min) was imposed up to the occurrence of the residual state condition, as is the case of tests 2-T, 3-B and 3-T. The tests 2-B, 2-M and 3-M were otherwise finished at axial strain values between 5.5% and 7%.

In Fig. 15, plots of q *versus* axial strain ε_a from the tests of the

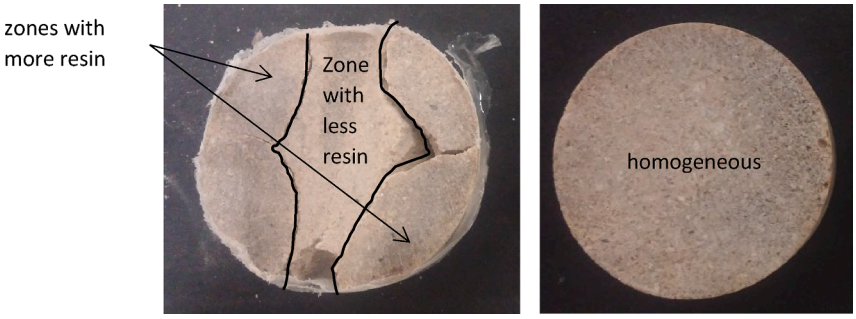

Fig. 11. Cut sections of specimens 1-VM1 (left) and 1-VT4 (right).

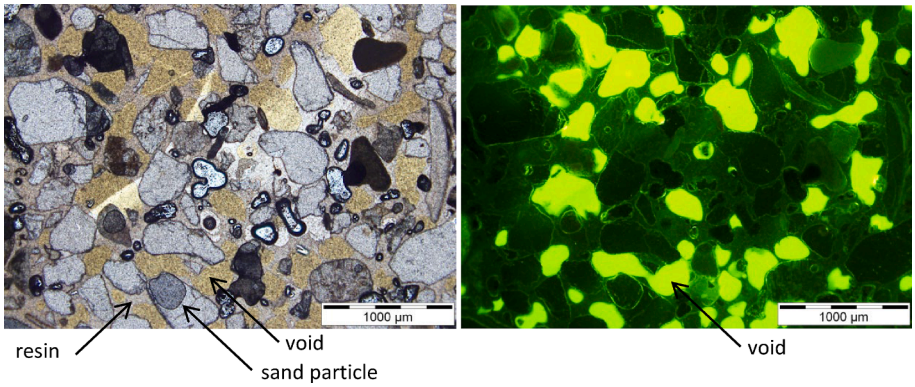

Fig. 12. Two different views of a selected zone from the laminar section of specimen 1-VM3.

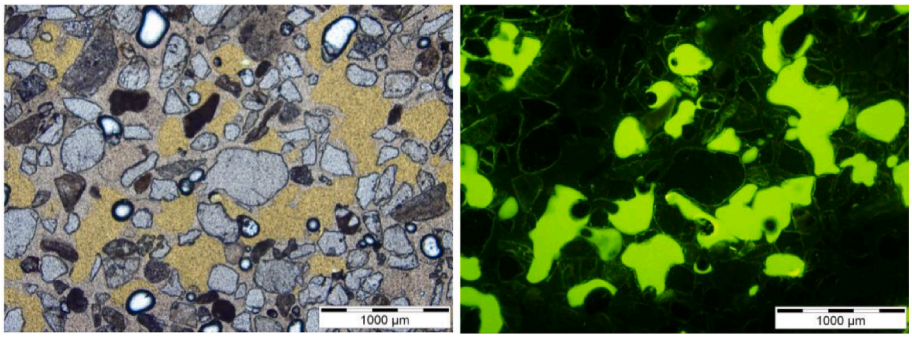

Fig. 13. Two different views of a selected zone from the laminar section of specimen 1-HB1.

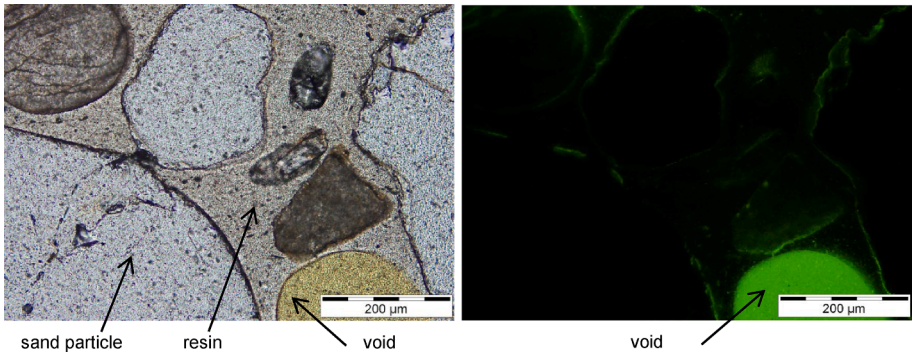

Fig. 14. Zoom of a selected zone from the laminar section of specimen 1-HB1.

Table 10
Triaxial compression testing of SRM specimens from sample #1: confining pressure, average strain rate, failure deviatoric stress and axial strain at failure.

Test	σ_3(MPa)	$\dot{\varepsilon}_{a;avg}$(%/min)	q_f(MPa)	$\varepsilon_{a,f}$(%)	Test	σ_3(MPa)	$\dot{\varepsilon}_{a;avg}$(%/min)	q_f(MPa)	$\varepsilon_{a,f}$(%)
1-VT5	0.3	0.25	24.5	1.6	1-HB5	0.3	0.35	19.7	1.1
1-VT7	1.2	0.40	27.4	1.9	1-HB8	1.2	0.53	25.2	1.4
1-VT6	2.0	0.30	30.8	2.3	1-HB4	2.0	0.40	29.5	1.3

Legend: σ_3 – confining pressure; $\dot{\varepsilon}_{a;avg}$ – average strain rate; q_f – failure deviatoric stress; $\varepsilon_{a,f}$ – axial strain at failure.

specimens of samples #2 (B, M and T) and #3 (B, M and T) are displayed. Concerning the peak shear strength, it occurred for axial strain values between 1% and 1.7%, with the exception of specimen 3-B, where a sudden decrease of deviatoric stress occurred at approximately 3% of axial strain. A possible explanation to this decrease could be related with significant heterogeneity of the specimen, which additionally could have favoured the breakage of structure bonds.

The residual state, with the axial strain occurring without increase of the deviatoric stress, could be identified in specimens 2-T and 3-T at approximately the same axial strain, i.e., 7%, with 15 MPa and 9 MPa as

Table 11
Triaxial compression testing of specimens from samples #2 and #3: confining pressure, estimates of small strain Young's modulus; peak and residual values of deviatoric stress.

Test	σ_3(MPa)	E(GPa)	q_{peak}(MPa)	$\varepsilon_{a,peak}$(%)	q_{res}(MPa)	Test	σ_3(MPa)	E(GPa)	q_{peak}(MPa)	$\varepsilon_{a,peak}$(%)	q_{res}(MPa)
2-T	0.3	3.93	28.9	1.2	14.7	3-T	0.3	7.15	40.3	1.1	8.5
2-M	1.2	7.13	47.0	1.3	16.5	3-M	1.2	4.01	45.1	1.7	13.1
2-B	2.0	4.54	36.2	1.6	24.9	3-B	2.0	4.68	40.7	2.1	19.3

Legend: σ_3 – confining pressure; E _ Young's modulus; q_{peak} – peak deviatoric stress; $\varepsilon_{a,peak}$ – axial strain at peak; q_{res} – residual deviatoric stress.

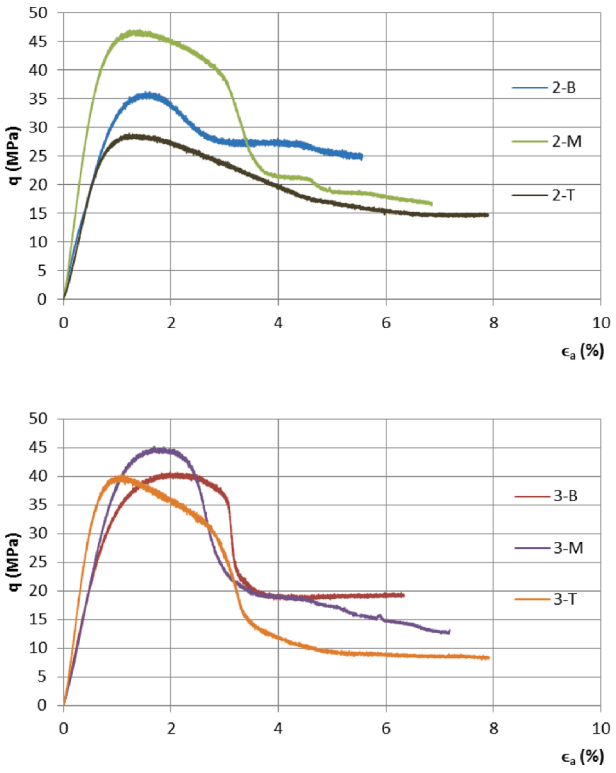

Fig. 15. Deviatoric stress *versus* axial strain results of triaxial tests of SRM specimens 2(-B, -M and -T) and 3(-B, -M and -T).

representative values of the prevailing deviatoric stress, respectively, as shown in Fig. 15.

In specimen 2-T, the failure pattern was formed by tension cracking of the top of the specimen. In the remaining specimens a well-defined shear band failure occurred. It is important to refer that, as specimens localized during failure, the measured residual parameters may not entirely reproduce the residual parameters at the shear plane [51,17].

Discussion of results

Regarding deformability, no indication was found that the humidity condition did introduce any significant difference between the estimates of the elastic deformability parameters, namely in the plausible sense that drying would provide a stiffer response, and of the uniaxial compressive strength, suggesting that the SRM may be studied as a soft rock.

A non-negligible dispersion of the Young's modulus value was obtained when considering the 14 results in Tables 9 and 11. This is due to the contrast in conditions of the specimens depending on the drilling direction and zone of provenience from the SRM columns. Yet, if one neglects the four extreme cases of specimens 1-VM1, 1-HB1, 2-M and 3-T the average value of E is equal to 4.9 GPa with a 14% coefficient of variation. This is considered currently a low dispersion of E in geological materials [24]. The mean value of the Poisson's ratio for the specimens in Table 9, not considering the above-mentioned outlier cases, is 0.24, with a CoV equal to 11%.

As shown in Table 10, during the load-controlled triaxial tests the SRM material exhibited predominantly a frictional response, i.e., q_f increased with increasing σ_3. The values of $\varepsilon_{a,f}$ are relatively small. The deviatoric stress q_f of specimen 1-VT5 is similar to the uniaxial strength of specimens 1-VM1 and 1-VM2. The same remark is valid for the specimen 1-HB5 and the pair of specimens 1-HB2 and 1-HB3.

Comparing the data in Tables 10 and 11, the q_{peak} results obtained in the triaxial compression tests are generally higher than the q_f values obtained with load-controlled tests of specimens from sample #1. Given the similarity of the strain rates in both types of tests, hypothetic strain rate effects could not be established.

Regarding the strain-controlled triaxial tests, illustrated in Fig. 15, in most of the cases the peak shear strength was displayed for axial strain values between 1% and 1.7%, with the exception of specimen 3-B. Although the SRM showed a relevant strength loss after the peak, a large plastic residual deformation was exhibited in this set of tests, with the material still retaining a significant strength. The suggestion that the SRM behaviour is similar to a soft rock's may also be drawn from the occurrence of small discrete drops of the mobilized q in the post-peak domain.

The higher values of the degree of homogeneity of the T and M specimens from both samples #2 and #3 are reflected in the increase of q_{peak} with the confining pressure, thus confirming the existence of a frictional component of shear strength. The B specimens, on the other hand, did not reflect the fact of being acted upon by the higher confinement pressure, which would be anticipated should their quality be similar to that of the T and M specimens.

The axial strain values at peak stress increase moderately for increasing values of the confining pressure and for increasing degree of homogeneity from the bottom to the top of the columns.

The residual strength envelope (RSE) considering specimens 2-T, 3-B and 3-T is displayed in Fig. 16 (blue filled dots). The estimated value of

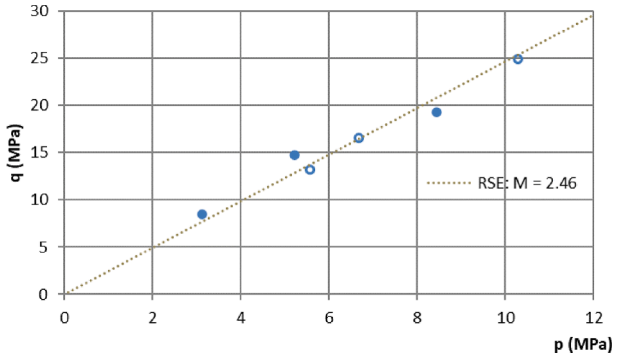

Fig. 16. Residual strength envelope considering specimens 2-T, 3-B and 3-T (blue filled dots) and final stress conditions of specimens 2-B, 2-M and 3-M (blue void dots).

the Mohr-Coulomb failure criteria strength parameter ϕ_r is equal to 60.8°. The blue void dots represent the final stress conditions of specimens 2-B, 2-M and 3-M, which match quite well the residual strength envelope. It is suggested that specimens 2-B, 2-M and 3-M, although ultimately not having reached residual state conditions, would have done so if the shearing had progressed.

For the peak state, considering the full set of uniaxial and triaxial compression tests of the SRM specimens, from samples #1, #2 and #3, the estimated values of the Mohr-Coulomb failure criteria strength parameters ϕ_p and c_p are equal to 62.5° and 2.4 MPa, respectively. The corresponding values for the triaxial tests only are of 67.2° and 0.5 MPa, respectively. The Cambridge representation of the peak states is displayed in Fig. 17 where, for the sake of comparison, the RSE is also shown.

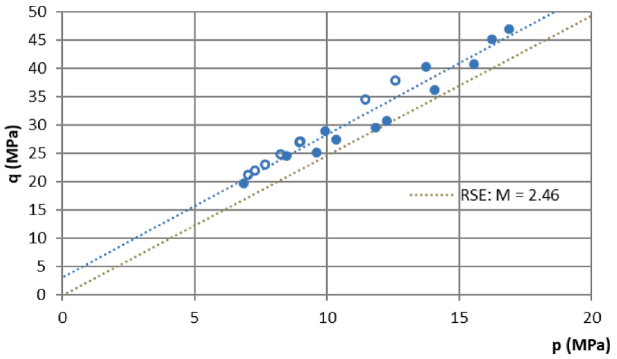

Fig. 17. Failure envelope for the peak mobilized shear strength on the full set of uniaxial (void blue dots) and triaxial (filled blue dots) compression tests.

Conclusions

The injection of a closed cell expansive polyurethane resin, MC-Injekt 2700 L®, in Tagus River sand, was tested at the laboratory as a ground improvement measure. Three injection tests were performed. The first consisted in injecting a central column of SRM and the second and third tests comprised injecting five separate columns each. A densification of the outlying sand was produced by the resin expansion in contact with water, corresponding to a maximum increase of 12% in the tested conditions. The expansion ratio of the performed injection tests was a direct consequence of water availability, i.e., of the contact surface area between the injected volume and the saturated sand.

The study of the physical properties of the SRM shows that the overall dispersion of dry density and of P and S waves' velocity is relatively small. Its permeability is five orders of magnitude less than the sand hydraulic conductivity, suggesting the filling of the most important voids of the sand, or the obstruction of the water access to these voids, by the hydrated resin.

Regarding the mechanical characteristics of the particle, the compressive strength was virtually not affected by the saturated or non-saturated conditions, contrasting with sandy particles. This important feature is justified by the single-phase behaviour of this material. An estimate of the uniaxial compressive strength, of 31.0 MPa in the vertical direction, and of 23.2 MPa in the horizontal direction, was determined in the uniaxial compression tests.

The studies of the SRM show damage and progressive loss of structure associated with loading, as is usual in cemented materials, which has a deleterious effect in the shear strength and eliminates the cohesion part for large strains, reaching a residual state. This allows concluding that, at the ultimate limit state, SRM is essentially a frictional material. Notwithstanding, the shear strength of the material can yet be considered very high when compared with the natural materials commonly used in civil engineering works.

For the peak state, considering the full set of uniaxial and triaxial compression tests of the SRM specimens, the estimated values of the Mohr-Coulomb failure criteria strength parameters ϕ_p and c_p are equal to 62.5° and 2.4 MPa, respectively. For the residual state, considering specimens 2-T, 3-B and 3-T, the estimated value of ϕ_r is equal to 60.8°. Due to the limitations of localized triaxial testing, this value of the residual friction angle shall not be extrapolated to design situations without further specific studies on possible scale effects.

Regarding stiffness, the comparison of the results reveals a similar performance to other ground improvement methods in the small strain domain, such as jet grouting, but with a notable essentially plastic behaviour for large deformations. A mean value of E of 4.9 GPa and an average value of ν of 0.24 was measured in the linear domain.

In terms of post peak stress–strain behaviour, the material must always be considered as a work softening material despite the confining pressures applied, as observed in the triaxial compression tests performed.

Funding

This work was supported by "Fundação para a Ciência e Tecnologia" (FCT) [grant number SFRH/BD/99581/2014].

CRediT authorship contribution statement

Luís Miranda: Conceptualization, Methodology, Formal analysis, Investigation, Writing – original draft, Visualization, Supervision. **Laura Caldeira:** Resources, Validation, Writing – review & editing, Project administration. **João Bilé Serra:** Resources, Validation, Writing – review & editing, Project administration. **Rui Carrilho Gomes:** Writing – review & editing.

Declaration of Competing Interest

The authors declare that they have no known competing financial interests or personal relationships that could have appeared to influence the work reported in this paper.

Data availability

The data used to support the findings of this study are included within the article.

Acknowledgments

The support and involvement of MC-Bauchemie Portugal, in particular Mr. Nuno Silva, are gratefully acknowledged. They were essential for the execution of the resin injections and of the preliminary adjustment testing, to determine the optimal injection solution for the sand container.

The sand material and the site investigation data were kindly provided by the Administração do Porto de Lisboa.

References

[1] Adalier K, Elgamal A, Martin G. Foundation liquefaction countermeasures for earth embankments. J Geotech Geoenviron Eng, ASCE 1998;124:500–17. https://doi.org/10.1061/(ASCE)1090-0241(1998)124:6(500).
[2] Ashford S, Rollins K, Bradford V, et al. Liquefaction mitigation using stone columns around deep foundations: full-scale test results. Transp Res Rec 2000;1736:110–8. https://doi.org/10.3141/1736-14.
[3] ASTM. D7012-14e1: Standard Test Methods for Compressive Strength and Elastic Moduli of Intact Rock Core Specimens under Varying States of Stress and Temperatures. ASTM International, West Conshohocken, PA, USA; 2014.
[4] ASTM. D4253-16: Standard Test Methods for Maximum Index Density and Unit Weight of Soils Using a Vibratory Table. ASTM International, West Conshohocken, PA, USA; 2016.
[5] ASTM. D4254-16: Standard Test Methods for Minimum Index Density and Unit Weight of Soils and Calculation of Relative Density. ASTM International, West Conshohocken, PA, USA; 2016.
[6] ASTM. D2487-17: Standard Practice for Classification of Soils for Engineering Purposes (Unified Soil Classification System). ASTM International, West Conshohocken, PA, USA; 2017.

[7] Baez J. A Design model for the reduction of soil liquefaction by vibro-stone columns. Los Angeles, CA, USA: University of Southern California; 1995. Ph.D. thesis.
[8] Bouckovalas G, Papadimitriou A, Niarchos D. Gravel drains for the remediation of liquefiable sites: the Seed & Booker (1977) approach revisited. In: Proc, international conference on performance-based design, CRC Press, Boca Raton; 2009.
[9] Boulanger R, Hayden R. Aspects of compaction grouting of liquefiable soil. J Geotech Eng, ASCE 1995;121:844–55. https://doi.org/10.1061/(ASCE)0733-9410(1995)121:12(844).
[10] Brennan A, Madabhushi S. Effectiveness of vertical drains in mitigation of liquefaction. Soil Dyn Earthq Eng 2002;22:1059–65. https://doi.org/10.1016/S0267-7261(02)00131-8.
[11] Conlee C, Gallagher P, Boulanger R, Kamai R. Centrifuge modeling for liquefaction mitigation using colloidal silica stabilizer. J Geotech Geoenviron Eng, ASCE 2012; 138:1334–45. https://doi.org/10.1061/(ASCE)GT.1943-5606.0000703.
[12] Cubrinowski M, Haskell J, Bradley B. Analysis and design of piles in liquefying soil. Project BIE 08/545. University of Canterbury, New Zealand; 2010.
[13] Erdemgil M, Saglam S, Bakir B. Utilization of highly expansive polymer injection to mitigate seismic foundation failure for existing structures. In: Proc, 8th Pacific conference on earthquake engineering, Nanyang Technological University, Singapore; 2007.
[14] Gallagher P, Conlee C, Rollins K. Full-scale field testing of colloidal silica grouting for mitigation of liquefaction risk. J Geotech Geoenviron Eng, ASCE 2007;133: 186–96. https://doi.org/10.1061/(ASCE)1090-0241(2007)133:2(186).
[15] Gallagher P, Pamuk A, Abdoun T. Stabilization of liquefiable soils using colloidal silica grout. J Mater Civ Eng, ASCE 2007;19:33–40. https://doi.org/10.1061/(ASCE)0899-1561(2007)19:1(33).
[16] Gatto M, Montrasio L, Berardengo M, Vanali M. Experimental analysis of the effects of a polyurethane foam on geotechnical seismic isolation. J Earthq Eng 2020. https://doi.org/10.1080/13632469.2020.1779871.
[17] Georgiannou VN, Burland JB. A laboratory study of post-rupture strength. Géotechnique 2001;51(8):665–75. https://doi.org/10.1680/geot.2001.51.8.665.
[18] Gohl W, Jefferies M, Howie J, Diggle D. Explosive compaction: design, implementation and effectiveness. Géotechnique 2000;50(6):657–65. https://doi.org/10.1680/geot.2000.50.6.657.
[19] Hamada M. Engineering for earthquake disaster mitigation. Springer. Maruzen Publishing Co. Ltd; 2013.
[20] He J, Vhu J, Ivanov V. Mitigation of liquefaction of saturated sand using biogas. Géotechnique 2013;63(4):267–75. https://doi.org/10.1680/geot.SIP13.P.004.
[21] Huang Y, Wen Z. Recent developments of soil improvement methods for seismic liquefaction mitigation. Nat Hazards 2015;76:1927–38. https://doi.org/10.1007/s11069-014-1558-9.
[22] ISO 527-1:2019: Plastics - Determination of tensile properties - Part 1: General principles. International Organization for Standardization, Geneva, Switzerland.
[23] Jakobsen UH, Brown DR. Reproducibility of w/c ratio determination from fluorescent impregnated thin sections. Cem Concr Res 2006;36(8):1567–73. https://doi.org/10.1016/j.cemconres.2006.05.003.
[24] Lee IK, White W, Ingles OG. Geotechnical engineering. Boston: Pitman; 1983.
[25] Lombardi D, Bhattacharya S. Liquefaction of soil in the Emilia-Romagna region after the 2012 Northern Italy earthquake sequence. Nat Hazards 2014;73:1749–70. https://doi.org/10.1007/s11069-014-1168-6.
[26] Manassero M, Boffa G, Dominijanni A, Puma S. Injection of expanding polyurethane resins. In: Proc, 24a Conferenze di Geotecnica di Torino. M. Manassero, A. Dominijanni, S. Foti, G. Musso, eds., Politecnico di Torino; 2016. p. 1–41.
[27] Martin J, Olgun C, Mitchell J, Durgunoglu H. High-modulus columns for liquefaction mitigation. J Geotech Geoenviron Eng, ASCE 2004;130:561–71. https://doi.org/10.1061/(ASCE)1090-0241(2004)130:6(561).
[28] Mashhoud H, Yin J, Panah A, et al. A 1-g shaking table investigation on response of a micropile system to earthquake excitation. Acta Geotech 2020;15:827–46. https://doi.org/10.1007/s11440-018-0742-6.
[29] MC-Bauchemie. Protection Technologies. Product Systems. Bottrop, Germany; 2014.
[30] McManus K, Charton G, Turner J. Effect of micropiles on seismic shear strain. In: Proc GeoSupport 2004, ASCE, Reston, Virginia, USA. p. 134–45.
[31] Miranda L. Liquefaction mitigation measures: prospective application to immersed tunnel foundations. Portugal: Universidade Técnica de Lisboa, Instituto Superior Técnico; 2019. Ph.D. thesis.
[32] Miranda L, Caldeira L, Serra J, Gomes R. Dynamic behaviour of Tagus River sand including liquefaction. Bull Earthquake Eng 2020; 18: 4581–604. Springer Nature. doi: 10.1007/s10518-020-00881-5.
[33] Mitchell J. Mitigation of liquefaction potential of silty sands. Proc., GeoCongress 2008, ASCE, Reston, Virginia, USA. p. 433–51.
[34] Moseley M, Kirsch K, editors. Ground improvement. 2nd ed. Abingdon, Oxon: Spoon Press; 2004.
[35] Mujah D, Shahin MA, Cheng L, et al. State-of-the-Art review of biocementation by microbially induced calcite precipitation (MICP) for soil stabilization. Geomicrobiol J 2017;34:524–37. https://doi.org/10.1080/01490451.2016.1225866.
[36] Nappa V. Soft grouting for seismic isolation: numerical and physical modelling. Italy: Università degli Studi di Napoli Federico II; 2017. Ph.D. Thesis.
[37] Nicholson P. Soil improvement and ground modification methods. Butterworth Heinemann; 2015. p. 129–33. ISBN 978-0-12-408076-8.
[38] Peng E, Zhang D. Prevention of liquefaction of saturated sand using biogas produced by pseudomonas stutzeri. DEStech Trans Mater Sci Eng 2017. https://doi.org/10.12783/dtmse/ictim2017/10182.
[39] Portugal J. Physical modelling with centrifuge (in Portuguese). Portugal: Universidade Técnica de Lisboa, Instituto Superior Técnico; 1999. Ph.D. thesis.
[40] Prabhakaran A, Kim K, Ebeido A et al. Polymer injection and associated site liquefaction remediation mechanisms. In: Proc, 17th world conference on earthquake engineering, Sendai, Japan; 2020.
[41] Rasouli R, Towhata I, Akima T. Experimental evaluation of drainage pipes as a mitigation against liquefaction-induced settlement of structures. J Geotech Geoenviron Eng, ASCE 2016:04016041. https://doi.org/10.1061/(ASCE)GT.1943-5606.0001509.
[42] Rasouli R, Towhata I, Hayashida T. Mitigation of seismic settlement of light surface structures by installation of sheet-pile walls around the foundation. Soil Dyn Earthq Eng 2015;72:108–18. https://doi.org/10.1016/j.soildyn.2015.02.010.
[43] Rayamajhi D, Nguyen T, Ashford S, et al. Numerical study of shear stress distribution for discrete columns in liquefiable soils. J Geotech Geoenviron Eng, ASCE 2014:04013034. https://doi.org/10.1061/(ASCE)GT.1943-5606.0000970.
[44] Ryan C, Jasperse B. Deep soil mixing at the Jackson Lake Dam. In: Proc, congress on foundation engineering: current principles and practice, ASCE Geotechnical Special Publication 1989; 22, F. Evanston and H. Kulhawy, eds., ASCE, Reston, Va., 1,354-367.
[45] Sabri MMS, Vatin NI, Alsaffar KAM. Soil injection technology using an expandable polyurethane resin: a review. Polymers 2021;13:3666.
[46] Sasaki Y, Taniguchi E. Shaking table tests on gravel drains to prevent liquefaction of sand deposits. Soils Found 1982;22:1–14.
[47] Saxena S, Reddy K, Avramidis A. Liquefaction resistance of artificially cemented sand. J. Geotech. Eng., ASCE, 1988; 114, 1395–1413. doi: 10.1061/(ASCE)0733-9410(1988)114:12(1395).
[48] Seed H, Booker J. Stabilization of potentially liquefiable sand deposits using gravel drains. J Geotech Eng Div, ASCE 1977;103:757–68.
[49] Skempton A. Standard penetration test procedures and the effects in sands of overburden pressure, relative density, particle size, ageing and overconsolidation. Géotechnique 1986;36:425–47. https://doi.org/10.1680/geot.1986.36.3.425.
[50] Soga K. Soil liquefaction effects observed in the Kobe earthquake of 1995. Proc, Inst Civil Eng - Geotech Eng 1998;131–1:34–51.
[51] Sulem J, Vardoulakis IG. Bifurcation analysis in geomechanics. CRC Press; 1995.
[52] Tokimatsu K, Yoshimi Y, Arizumi K. Evaluation of liquefaction resistance of sand improved by deep vibratory compaction. Soils Found 1990;30:153–8.
[53] Towhata I. Geotechnical earthquake engineering. Berlin/Heidelberg, Germany: Springer-Verlag; 2008.
[54] Traylen N. Resin injection ground improvement research trials. New Zealand: Geotech Consulting ltd. Christchurch; 2017.
[55] Uretek Worldwide. FAQ - about URETEK solutions. http://www.uretekworldwide.com/, 2014 (accessed 18 January 2019).
[56] Verdugo R, González J. Liquefaction-induced ground damages during the 2010 Chile earthquake. Soil Dyn Earthq Eng 2015;79:280–95. https://doi.org/10.1016/j.soildyn.2015.04.016.
[57] Walton G, Labrie D, Alejano LR. On the Residual Strength of Rocks and Rockmasses. Rock Mech Rock Eng 2019;52:4821–33. https://doi.org/10.1007/s00603-019-01879-5.
[58] Yang Y, Ruan S, Wu S, et al. Biocarbonation of reactive magnesia for soil improvement. Acta Geotech 2021;16:1113–25. https://doi.org/10.1007/s11440-020-01093-6.
[59] Zeybek A, Madabhushi S. Influence of air injection on the liquefaction-induced deformation mechanisms beneath shallow foundations. Soil Dyn Earthq Eng 2017; 97:266–76. https://doi.org/10.1016/j.soildyn.2017.03.018.

Luís Miranda is an Auxiliary Researcher in the Geotechnics Department of the National Laboratory for Civil Engineering (LNEC). In 2019, he completed his Ph.D. in civil engineering at IST, Universidade de Lisboa, entitled: "Liquefaction Mitigation Measures: Prospective Application to Immersed Tunnel Foundations", where he also lectured the course "Geotechnical Structures Analysis". His research is centred on physical and numerical modelling of the behaviour of geomaterials in underground works, particularly related with the study of liquefaction and mitigation measures, as well as geotechnical variability. He worked as a designer of bridges and special structures at GRID, International Consulting Engineers.

Laura Caldeira is a Principal Researcher and President of the National Laboratory for Civil Engineering (LNEC). She completed her Ph.D. in civil engineering in 1994, at FEUP, Universidade do Porto, entitled "Dynamic Analysis of Embankment Dams. Assessment Methods", her Habilitation in the scientific area of Soil Mechanics in 2006, and her Aggregation in civil engineering in 2013. She was a Full Professor at IST, Universidade de Lisboa, between 2008 and 2017. Her research interests include geotechnics, embankment dams, constitutive models, laboratory and in situ characterization of soils, risk management, seismic risk, and observation and behaviour of geotechnical structures.

João Bilé Serra is a Principal Researcher and Head of the Geotechnics Department of the National Laboratory for Civil Engineering (LNEC). He completed his Ph.D. in civil engineering in 1998, at IST, Universidade de Lisboa, entitled "Experimental characterization and numerical modelling of the cyclic behaviour of non-cohesive soils. Application to Earthquake Engineering", and his Habilitation in the scientific area of Soil Mechanics in 2020. He is an Associate Professor at FCT, Universidade Nova de Lisboa. His main research subjects include safety and risk management in geotechnics, with greater emphasis on landfill dams, geotechnical seismic engineering, tunnels and underground works.

Rui Carrilho Gomes is an Assistant Professor of Geotechnics in the Civil Engineering Department at Instituto Superior Técnico, University of Lisbon. He completed his Ph.D. in civil engineering in 2009, at IST, Universidade de Lisboa, entitled "Numerical modelling of the seismic response of the ground and of circular tunnels". His research focuses on numerical modelling of seismic site effects and geotechnical structures, seismic microzonation and seismic surface methods. He is the coordinator of the Interreg Atlantic Area-funded AGEO - Platform for Atlantic Geohazard Risk Management.